ACS Photonics

pubs.acs.org/journal/apchd5

Article

Origin of Gouy Phase Shift Identified by Laser-Generated Focused Ultrasound

Taehwa Lee, Yeonjoon Cheong, Hyoung Won Baac, and L. Jay Guo*

Cite This: https://dx.doi.org/10.1021/acsphotonics.0c01313

Read Online

ACCESS | Metrics & More | Article Recommendations | Supporting Information

ABSTRACT: The Gouy phase shift, the phase change of a converging wave passing through a focus, is a general characteristic of waves of any kind, including light and sound. Direct observation of the phase shift has been typically limited to high-frequency short pulses, e.g., terahertz light pulses and picosecond sound pulses. We demonstrate the Gouy phase shift of relatively low-frequency, megahertz ultrasound, widely implemented for ultrasound imaging and sensing. This demonstration is experimentally enabled with monopolar ultrasound pulses generated by nanosecond laser excitation of a light-absorbing concave film, which undergoes polarity reversal from before to after focusing. Moreover, our simulation results for various input pressure profiles show that the Gouy phase shift is observed for beams with significant diffractions. The physical origin of the phase anomaly is intuitively explained based on Huygens' principle and the acoustic interference of secondary waves, providing further understanding of the Gouy phase shift in optics as well.

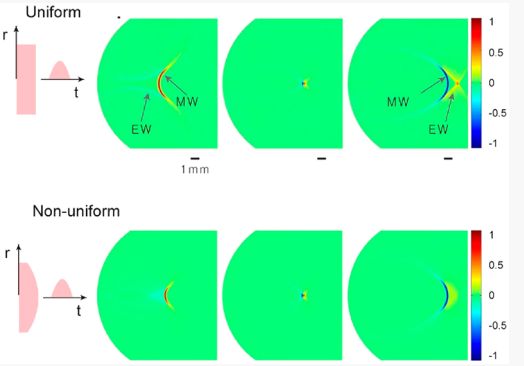

KEYWORDS: *Gouy phase shift, laser ultrasound, photoacoustics, megahertz, Huygens' principle*

INTRODUCTION

A spherical converging wave propagating through a focus experiences a π phase shift, known as the Gouy phase shift, with respect to a reference plane wave or a carrier envelope.[1] The Gouy phase shift has practical implications, e.g., for design of laser resonant cavities.[2] Since Gouy's original demonstration by showing interference between a converging light and a reference plane light, the phase anomaly has been the subject of study for decades,[3−7] aiming to understand its physical origin and to observe it by using noninterference methods.[6,8−11] For example, direct, noninterferometric observation of such a phase shift was permitted for single-cycle terahertz pulses, unambiguously demonstrating the polarity reversal as a result of the Gouy phase shift.[6,8,9] Even for few-cycle laser pulses, the phase anomaly was observed with respect to their carrier envelope owing to stabilization of the carrier-envelope phase.[10] In addition, there is a myriad of evidence that the Gouy phase shift is a universal phenomenon for all focused waves including nondiffracting beams (e.g., Airy and Bessel beams),[12−15] radially polarized beams,[16,17] and vortex beams.[18,19] Also, the Gouy phase shift is accumulated while a beam propagates plural optical components.[20]

Despite the rich experimental observations, the physical origin of the phase anomaly continues to be a topic of discussion, leading to many postulations. For example, the phase anomaly was explained by the transverse confinement and the uncertainty principle in quantum mechanics.[5,21] In another study, the phase shift is related to the discontinuities in the angular spectrum.[22] Some earlier studies tried to provide intuitive explanation of the Gouy phase shift by using geometrical properties of Gaussian beams,[4,23] Berry's geometrical phase,[24] and the tilted wave vectors.[25]

In acoustics, the observation and practical uses of the Gouy phase shift has rarely been investigated. Particularly, observation of the π phase shift in three-dimensional (3D) focusing has not been reported, as it was limited to a $\pi/2$ phase shift enabled by a plane wave[26] or a circular surface wave.[27] In these works, the phase shifts were demonstrated with high-frequency acoustic pulses (picosecond ultrasonics) that were generated by femtosecond laser excitation of planar acoustic sources. Although in theory the Gouy phase shift is observable in any frequency regimes, the phase anomaly has not been experimentally demonstrated for relatively low frequencies of megahertz ultrasound—a scientifically rich frequency band used for medical ultrasound, and nondestructive test and evaluation.

Recently developed photoacoustic (PA) transmitters capable of producing tightly focused short megahertz ultrasound pulses[28−31] provide a possible platform to investigate the

Received: August 20, 2020

acoustic Gouy phase shifts in 3D. Moreover, the photoacoustic pulses generated by these PA transmitters and pulse lasers are known to have positive (compressive) monopolar waveforms in the near field before reaching the focal point.[32−34] In this work, we experimentally demonstrate a direct observation of the Gouy phase shift with focused ultrasound pulses of megahertz frequencies, exhibiting polarity reversal from positive to negative after passing through a focus. The direct observation in the relatively low frequency band is enabled by single-cycle, tightly focused ultrasound pulses that are generated by pulsed optical excitation of a photoacoustic coating on a concave surface. By using the Huygens' concept of secondary waves and the Rayleigh integral, the physical origin of the phase anomaly is intuitively explained. We find that the phase shift is strongly correlated with the sequence change in secondary waves and their spread along the propagation axis. The negative monopolar pulses by the acoustic Gouy phase shift can be useful for fundamental mechanism studies in biomedical engineering, e.g., elucidating interaction between mechanical waves and tissue.

RESULTS AND DISCUSSION

Direct Observation of Gouy Phase Shift. To answer the question whether the Gouy phase shift is observable in relatively low frequencies such as megahertz (MHz) or lower acoustic frequencies, we start by considering a focusing Gaussian beam, whose phase shift is characterized by[41]

$$\phi(z) = \tan^{-1}\left(\frac{z}{z_R}\right) \tag{1}$$

where z is the distance along the propagation axis, $z = 0$ at the focus, and z_R is the Rayleigh length $\left(z_R = \frac{\pi f w_0^2}{c}\right)$ with w_0 being the beam waist at the focus, c the wave speed, and f the frequency. From eq 1, it is clear that a π phase shift between two points before and after the focus ($z = \pm z_0$; $z_0 > 0$) requires $z_0 \gg z_R$, i.e., $\phi(z_0) - \phi(-z_0) = \pi/2 - (-\pi/2) = \pi$, indicating that small z_R (i.e., tight focusing) allows a drastic phase shift near the focus. Thus, whether the phase shift is observable or not critically depends on the Rayleigh length, which is order of c/f by assuming diffraction-limited beam waist ($w_0 \geq 2\lambda/\pi$ with λ being the wavelength).[2] Interestingly, the Rayleigh length of THz (10^{12} Hz) light is comparable to that of MHz ultrasound (>10^7 Hz) in water, that is, $z_R \propto c/f \sim 10^2$ μm because of the large difference in the speeds of sound in water and light, $c_{light}/c_{sound} \sim 10^5$. In this regard, the Gouy phase shift can be experimentally observed by using tens of MHz ultrasound.

From eq 1, the phase shift $\phi(z)$ is found to be frequency-dependent. Thus, focusing of a broadband pulse composed of multiple frequency components leads to a polarity-reversed pulse, which is a combined effect of the constituent frequencies each featuring a π phase shift over a different distance.[6] It is well-known that the polarity reversal of a broadband light pulse enables its direct observation (i.e., via noninterferometric methods).[6] To demonstrate the Gouy phase shift-induced polarity reversal in MHz ultrasound, we use broadband ultrasound pulses produced by a photoacoustic (PA) lens and a pulse laser.[28] The broadband ultrasound generated by a pulse laser of a Gaussian temporal profile features positive monopolar pulses, the temporal profile of which is determined by that of the laser pulse. Here, the PA lens consists of a transparent plano-concave lens (focal length l_f = 9.2 mm and diameter D = 15 mm) and a carbon nanotube (CNT) composite coated on the concave side,[28] as illustrated in Figure 1. Nanosecond laser excitation of the CNT composite film

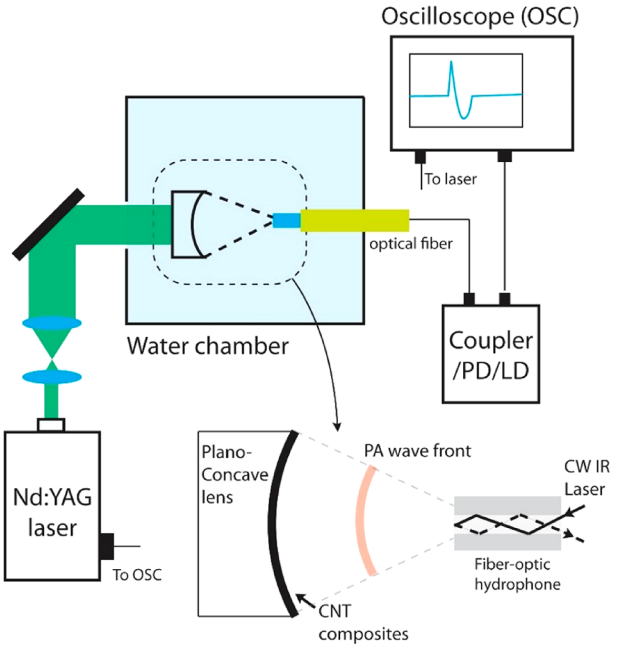

Figure 1. Experimental setup of focused photoacoustic (PA) wave generation consisting of pulsed Nd:YAG laser (pulse duration: 6 ns) and a optically transparent plano-concave lens with a carbon nanotube (CNT)-PDMS composite coating. Pulsed optical excitation of the CNT-PDMS composite film coated on the concave surface generates PA waves converging to the focus (i.e., the center of the curvature of the concave surface). The waveforms are measured with a broadband fiber-optic hydrophone (photodetector bandwidth of >70 MHz).

generates converging broadband pulses, whose center frequency is measured to be f_c = 15 MHz (measured at the focus). The focal waveforms are directly characterized by a broadband point detector consisting of a single-mode optical fiber with a core diameter of 6 μm. In addition, the wave propagation is visualized by using laser flash shadowgraphy[42] (see Experimental Setup for more details). To simulate the acoustic wave propagation, a full wave simulation is conducted to solve the time-dependent wave equation subject to a pressure source with a Gaussian temporal profile on the concave surface, $p_0(r, t) = A(r)e^{-t^2/t_d^2}$, where $A(r)$ is the lateral source pressure profile with r being the distance from the propagation axis, and t_d is the pulse duration ($t_d = 1/2f_c$) (see Numerical Simulation for more details). The lateral pressure source profile is expressed by $A(r) = \cos\theta_F = \sqrt{1 - (r/l_f)^2}$ where l_f is the focal length and θ_F is the angle between the laser beam and the surface normal so as to consider the actual laser fluence on the CNT film that is reduced by the cosine of the angle (θ_F).

Figure 2a exhibits the axisymmetric simulation results, showing the wave fronts first converging to the focus and then diverging from it. The pressure field at each time instant is normalized to the peak pressure amplitude. The photoacoustic wave leaving the concave PA layer is tightly focused on a spot due to the large lens diameter (D = 15 mm) relative to the

https://dx.doi.org/10.1021/acsphotonics.0c01313
ACS Photonics XXXX, XXX, XXX−XXX

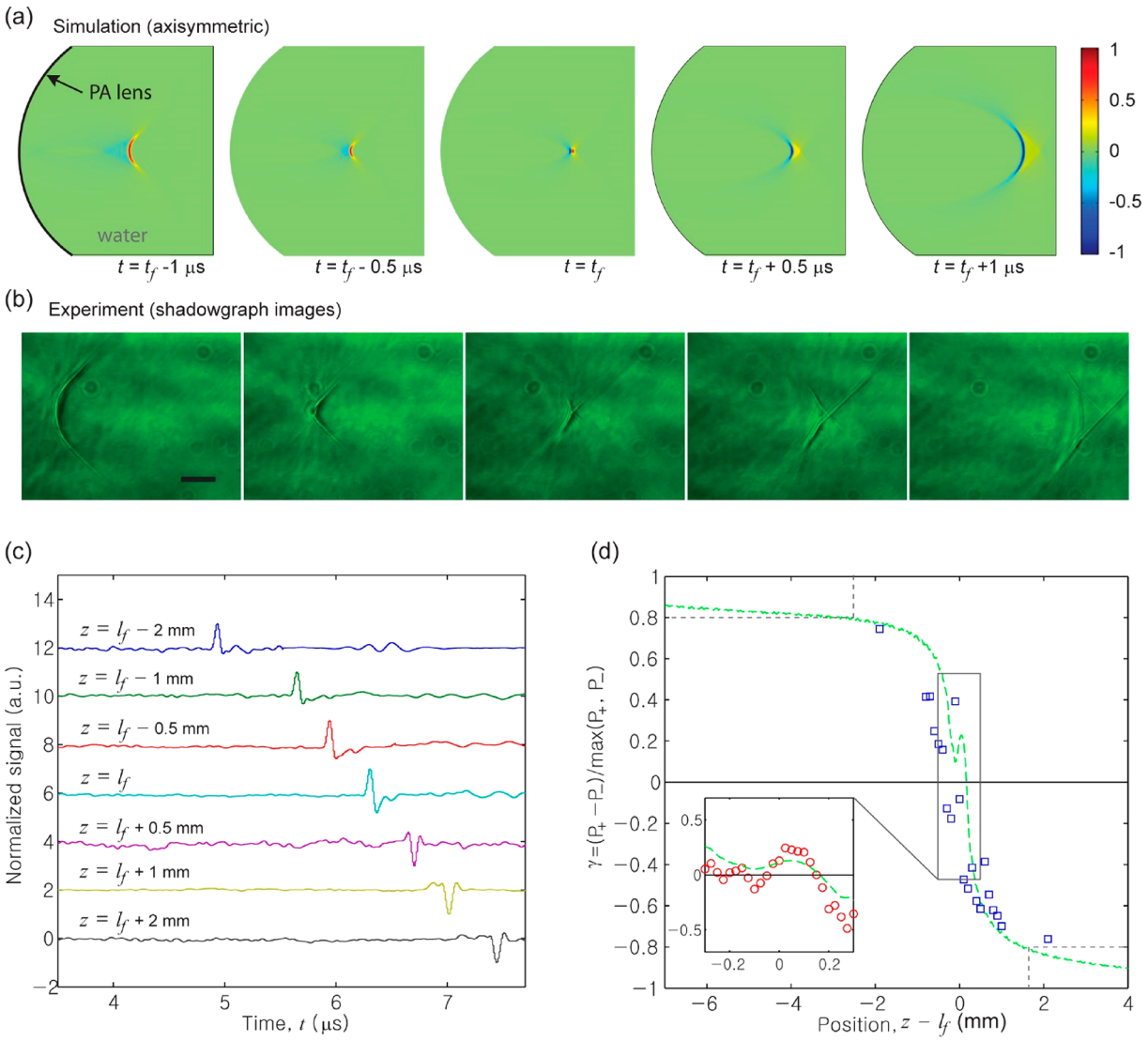

Figure 2. (a) Simulation of photoacoustic wave propagation (normalized to the peak amplitude). Time is set to zero when the wave crosses the focal point. The time interval between the snap shots is 0.5 μs. The collimated laser beam is incident on the concave surface with an angle (θ_F) depending on r. (b) Time-resolved shadowgraph images of the wave fronts near the focus. The time interval between the images is 0.07 μs. The scale bar indicates 100 μm. (c) Measured photoacoustic transients by the point detector at the different points along the propagation axis (i.e., r = 0). (d) Ideality factors of the measured photoacoustic signals. The ideality factor (γ) represents the polarity of the signals (γ = 1 for positive monopolar, π = 0 for bipolar, and γ = −1 for negative monopolar), which is defined as $\gamma = (P_+ - P_-)/\max(P_+, P_-)$ with P_+, P_- being the positive and negative peak amplitudes, respectively. The dashed green line represents the simulation, while the symbols (blue squares and red circles) indicate the measurements. The blue square symbols indicate measurement with a scan spacing of Δz = 100 μm for z = 2 mm. The red circle symbols in the inset shows the measurements in the zoomed region near the focus (a scan spacing of Δz = 25 μm).

short focal length l_f (9.2 mm) (i.e., low f-number of l_f/D = 0.61).[31] Note that the simulated wave fronts show the distinct color change from red (before focusing) to blue (after focusing), that is, polarity reversal from positive to negative polarity. The polarity reversal seen in this simulation is a direct indication of the Gouy phase shift of the broadband pulses. The triangular shade next to the wave fronts arises because of the nonuniform pressure source profile (detailed discussion will follow in the next section).

We experimentally observed the Gouy phase shift-induced polarity reversal. First, the shadowgraph images show a noticeable contrast change, as shown in Figure 2b. The diverging wavefront after the focus (negative polarity) is less discernible, whereas the converging wavefront (positive polarity) shows the sharp line, confirming the polarity reversal (Supporting Information for Note 1). Figure 2c shows the waveforms measured at different locations along the propagation axis, each waveform normalized to its peak amplitude. The measured waveforms show the polarity reversal from positive (see at $z = l_f$ − 2 mm) to negative ($z = l_f$ + 2 mm), corresponding to a change from compressive to tensile wave. The positive monopolar pulses at the locations ($z < l_f$) are similar to the temporal profile of the laser excitation when the PA film is much thinner than the acoustic penetration depth.[32] We should point out that our earlier publication on the PA lens reported the bipolar waveform at the focus ($z = l_f$) and was not able to observe a polarity reversal due to relatively weak focusing (a PA lens of a relatively high f-number >0.9).[28]

To quantify the polarity evolution along the propagation axis, we define an ideality factor (γ) given by

https://dx.doi.org/10.1021/acsphotonics.0c01313
ACS Photonics XXXX, XXX, XXX−XXX

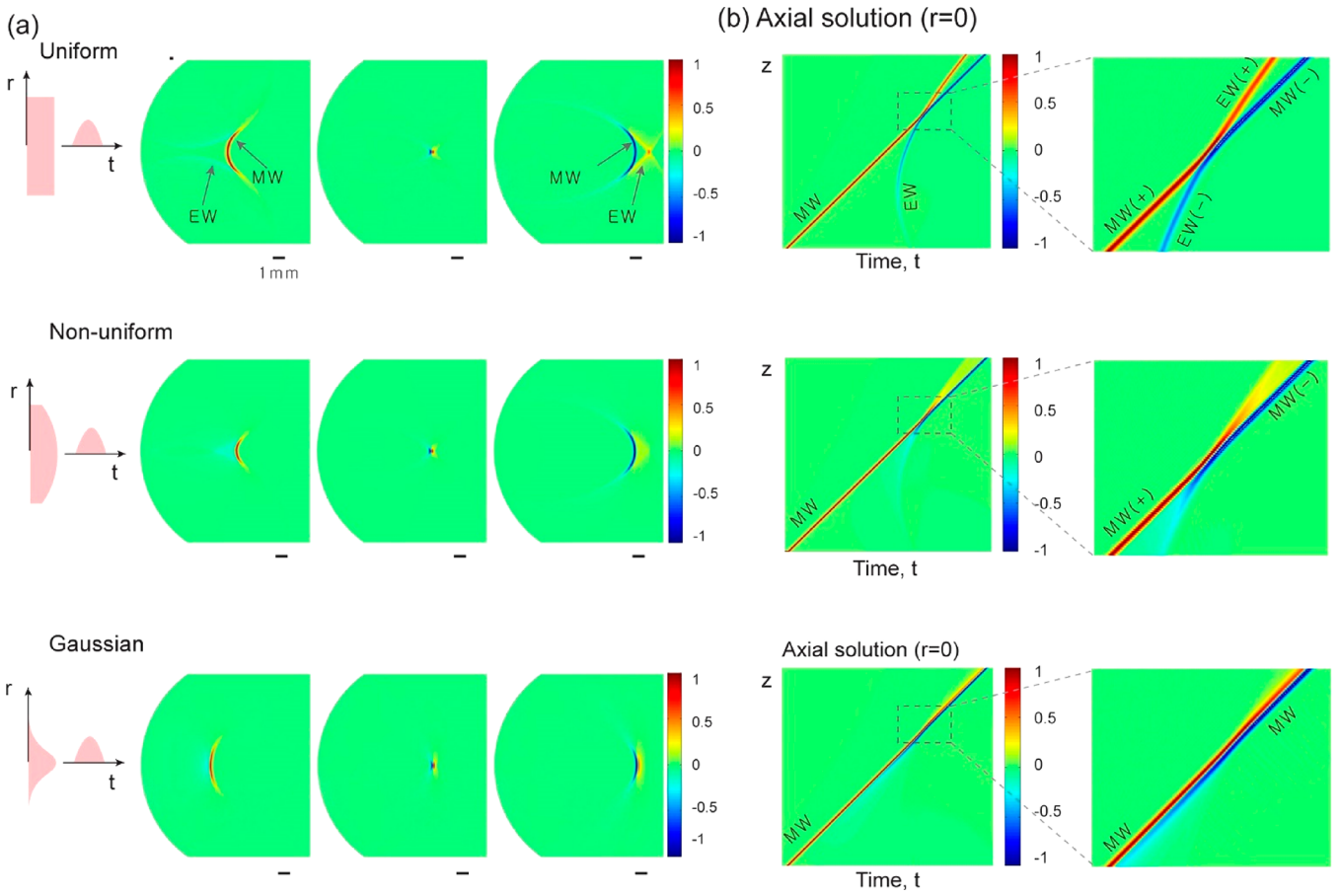

Figure 3. Axisymmetric full wave simulation for three different transverse pressure profiles (uniform, nonuniform, and Gaussian). (a) Wave propagation. For all the pressure profiles, the main wave fronts resembling the shape of the PA lens propagate, converge, and reverse their sign of radius of curvature. Notably, regardless of the profiles, polarity reversal from positive to negative is seen through color change from red to blue. For the uniform pressure profile, besides the main wave (MW) front, diffraction-induced edge wave (EW) front is seen. The scale bar shows 1 mm, corresponding to approximately 10λ and $4z_R$. (b) Axial solutions ($r = 0$) and zoomed regions near the focus. The main front is represented as a straight line, showing the distinct color change. The diffraction wave for the uniform case is represented as a curved line. From the zoomed plots, the polarity reversal for the uniform case occurs more sharply than those for the other cases.

$$\gamma(z) = \frac{(P_+ - P_-)}{\max(P_+, P_-)} \tag{2}$$

where P_+ and P_- are the positive and negative amplitudes, respectively. The ideality factor ranges from -1 to 1, representing the evolution from positive monopolar waveform for r $\gamma \approx 1$ ($P_+ \gg P_-$), through the transition of bipolar waveform for $\gamma = 0$ ($P_+ = P_-$) to negative monopolar waveform for$\gamma \approx -1$ ($P_+ \gg P_-$). As shown in Figure 2d, the ideality factor abruptly changes within a short-range of 1 mm [about four times the Rayleigh length, $z_R = \pi w_0^2/(c/f_c) = 250$ μm for a 6-dB lateral beam width (w_0)) of 90 μm]. Note that the polarity evolution is found to be asymmetric, i.e., $\gamma(+z_0) \neq \gamma(-z_0)$. Such asymmetric polarity evolution, which is in a sharp contrast to symmetric one in optics, is explained by the fact that the photoacoustic waves are emitted from the sound-reflecting concave surface (PA lens). The simulation results (green dashed line) shows a good agreement with the measurement results (symbols) for a scan spacing of $\Delta z = 100$ μm. The inset of Figure 2d shows the polarity near the focus, which was recorded in a separate measurement using a smaller scan spacing Δz. Because of the nonlinear effect, the measured values (red symbols) at the focus are higher than the simulation results based on linear wave propagation.

Intuitive Explanation of the Phase Shift. The observed acoustic polarity reversal is based on the photoacoustic beam of nonuniform amplitudes along the transverse direction [i.e., $A(r) = \cos\theta_F$], which is different from the optical Gouy phase shift relying on a Gaussian beam. To see the effect of the lateral profile on the phase shift, we additionally conduct simulations for two other lateral profiles (uniform and Gaussian), as shown in Figure 3. These beams of three lateral profiles result in significant wave diffraction, compared to diffraction-free solutions (e.g., Bessel beam) of the wave equation. Regardless of the lateral profiles, we observe the polarity reversal, i.e., the color change of the wavefront from red to blue. Thus, our findings indicate that the Gouy phase shift is observable in beams with large diffraction, confirming that the phase anomaly reflects a general characteristics of focusing waves of any lateral profiles.

Unlike Gaussian beams, the non-Gaussian acoustic beams (with either uniform and nonuniform amplitude) provide further understanding of the Gouy phase shift by producing the diffraction waves. For the uniform beam (Figure 3a), the diffraction waves originating from the edges of the PA lens are very distinct due to the equal amplitude of the secondary waves. Interestingly, these diffraction waves also experience polarity reversals. Here, the diffraction waves from the edges

https://dx.doi.org/10.1021/acsphotonics.0c01313
ACS Photonics XXXX, XXX, XXX−XXX

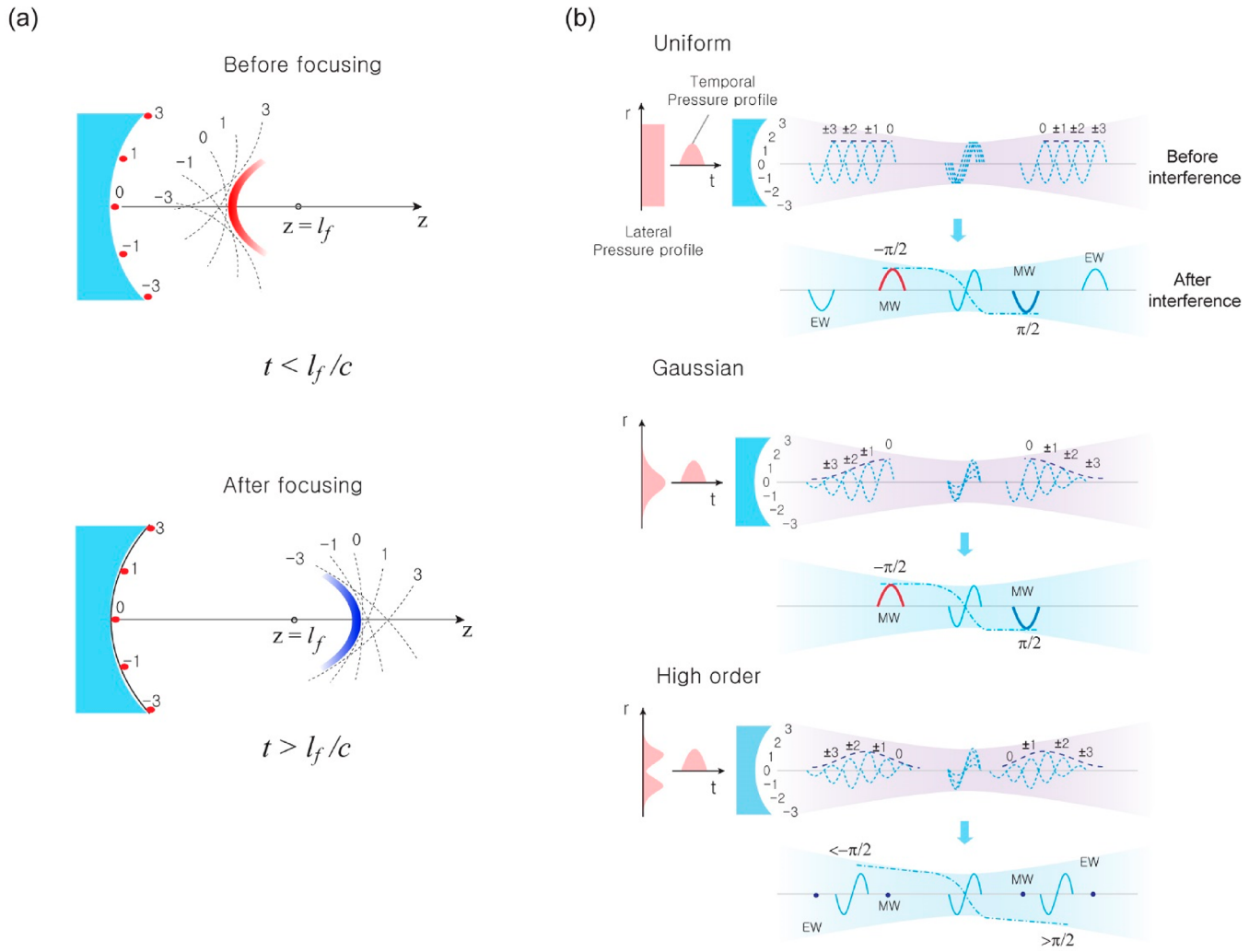

Figure 4. (a) Huygens' picture showing wave fronts constructed spherical secondary waves labeled as the number corresponding to the point sources on the concave surface. The wave fronts are constructed for two different radii, respectively ($ct < l_f$ and $ct > l_f$). The resulting wave fronts exhibit the sign change of radius of curvature. Note that the secondary waves are spread on the axis, experiencing axial order change. (b) The secondary waves on the axis (top) and the resulting waves (bottom) for the three lateral pressure profiles. The secondary waves are spread along the axis, each secondary wave represented as a bipolar waveform with a leading positive phase and a trailing negative phase. As a result of interference of the secondary waves, the polarity of the wave fronts is determined, providing the physical explanation of phase shift.

are referred to as the edge waves (EWs),[43] while the main wave fronts resembling the concave surface is referred to as the main waves (MWs). Notably, the EWs initially lag behind the MWs, but they advance the MWs after the focus. Such an axial order change is closely related to the polarity reversal of the waveform, and is hidden for a Gaussian beam because of diminishing amplitude of the EWs. To understand the characteristics of the EWs, we plot the axial pressure transients at different z locations, i.e., $p(r = 0, z, t)$, as shown in Figure 3b. The EWs are characterized by curves crossing the straight lines ($z = ct$) of MWs at the focus.

The axial order change between the MW and EW is evident from the Huygens' principle. As depicted in Figure 4a, Huygens' picture states that the MW fronts (red/blue arcs) are constructed by the envelope of the secondary spherical waves (dashed lines) of the same radius ($R_{SW} = ct$) emanating from source points on the concave surface of the PA lens. Each secondary wave and its corresponding source point are denoted as 0, ±1, or ±3. For $t > l_f/c$ (i.e., $R_{SW} > l_f$), the diverging MW (blue arc) lags all the secondary waves on the z axis. Particularly, the secondary waves from the edges (±3) advance the most, leading to the EWs [see Figure 3a].

To determine the polarity of the wave fronts, we consider superposition of these secondary waves on the z-axis. Figure 4b illustrates the secondary waves arriving the z-axis from each source point before and after passing the focal point (top panel); their destructive interference produces the final observable waveforms (bottom panel), as shown for three lateral profiles: uniform, Gaussian, and high-order profiles. At three time instants ($t < l_f/c$, $t = l_f/c$, and $t > l_f/c$), we consider the secondary waves on the z axis, each represented as a bipolar pulse (i.e., dp_s/dt, time-derivative of the positive monopolar point source $p_s \propto e^{-t^2/t_d^2}$).[32] At $t = l_f/c$, all the secondary waves arrive to the focus, resulting in a bipolar pulse. At $t < l_f/c$ or $t > l_f/c$, the secondary waves are found to spread along the z axis because of $l_f \neq R_{SW}$ ($= ct$). For the uniform lateral profile, the secondary waves of the same amplitude (spread along the z axis between $z_1 < z < z_2$) interfere, which is modeled by the Rayleigh integral:

https://dx.doi.org/10.1021/acsphotonics.0c01313
ACS Photonics XXXX, XXX, XXX−XXX

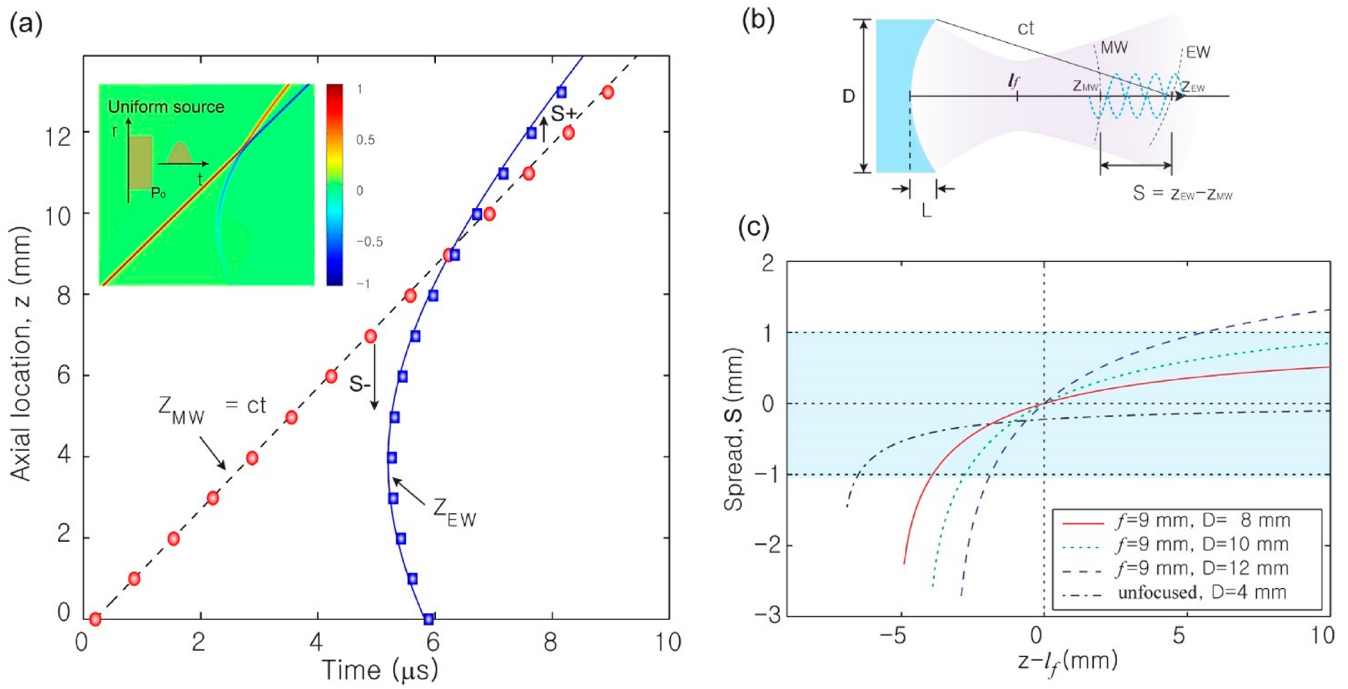

Figure 5. (a) Locations of the main wave (MW) and edge wave (EW) fronts on the z axis for the uniform lateral profile. The MW is characterized by a straight line ($z_{MW} = ct$), whereas the EW is identified as a curved line (z_{EW}). The curved line of z_{EW} crosses the straight line of z_{MW} at $z = l_f$. The lines indicate the geometrically calculated locations, while the symbols represent the simulation results. The inset shows the axial solutions (Figure 3b) used for extraction of the axial locations. (b) Illustration of the longitudinal separation (S) of the secondary wave on the axis between the MW and EW, i.e., $S = z_{EW} - z_{MW}$. The locations z_{EW} correspond to the crossing points of the z axis and the circle of a radius ct and a center ($r = D/2$, $z = L$). (c) Geometrically calculated separation (S) for different lens diameters (D) and the same focal length (l_f). The separation (S) approaches zero at the focus. For the unfocused pressure source, the spread (S) asymptotically approaches zero.

$$\int_{z_1}^{z_2} (\mathrm{d}p_s/\mathrm{d}t)\left(\frac{\mathrm{d}t}{\mathrm{d}z}\right)\mathrm{d}z \propto p_{s,z_2} - p_{s,z_1} \tag{3}$$

Eq 3 indicates that the leading pulse at $z = z_2$ has a positive polarity ($+p_s$), whereas the trailing pulse at $z = z_1$ has negative polarity ($-p_s$) (see Supporting Information for Note 2). Thus, the polarity depends on whether it is a trailing or leading pulse. In this aspect, it is clear that the polarity reversal of the wave fronts occurs after passing through the focus, because the wave fronts experience the axial order change from a leading position to a trailing position.

For the Gaussian lateral profile, the interference of the secondary waves results in only the MWs, and the EWs are diminished due to the much lower source intensity at the edge. Without the EWs, the axial order change of the MW cannot be explicitly observed, but it can be seen from the Huygens' picture (see Figure 4b). It is noted that for higher-order beams having the peak intensity between the sources ±1 and ±2, the wavefront on the z axis (z_p) is located between the MW (from the source 0) and EW (from the sources ±3), leading to deviation from the MW ($z = ct$). This deviation from the MW introduces an additional propagation phase, enabling a phase shift exceeding π.

Axial Spread of the Secondary Waves. The polarity reversal (the color change of the straight line) is clearly observed, when for the uniform lateral profile, the curved line of the EWs is completely separated from the straight line of the MWs [see Figure 3b]. This observation suggests that such a separation can be used to quantify the phase shift. As illustrated in Figure 5b, the separation between the MW and EW on the z axis is represented by

$$S(t) = z_{EW} - z_{MW} \tag{4}$$

where z_{MW} is given by $z_{MW}(t) = ct$, and z_{EW} is expressed by $z_{EW} = L + \sqrt{(ct)^2 - (D/2)^2}$ with L being the depth of the concave surface of the PA lens. The analytically calculated axial locations (lines), z_{EW} and z_{MW}, show an excellent agreement with those from the simulated axial solution (symbols), as seen in Figure 5a. For different diameters (D) and the same focal length (l_f), the separation $S(t)$ is plotted in Figure 5c. We observe that the larger the diameters D are, the more abrupt the separation occurs, explaining why the tight focusing through a small $f\# = l_f/D$ exhibits a more drastic phase shift. In the far field, the separations of the focused beams asymptotically approach the depth (L) of the PA lens [i.e., $S(t) \to L$], whereas that of the unfocused beam reaches zero with no sign change.

An additional requirement for the distinct polarity reversal is that from an interference perspective, the separation $S(t)$ should be much greater than the wavelength ($\lambda = c/f_c$), i.e., $S/\lambda \gg 1$. This requirement is reasonable, as we find that the separation relative to the wavelength(S/λ) is physically equivalent to z/z_R in eq 1 (see Supporting Information for Note 3). However, the acoustic phase shift by the PA lens cannot be simply described by the arctangent function $\tan^{-1}(S/\lambda)$ because of the unique characteristic of the asymmetrical phase shift [γ ($+ z_0$) $\neq \gamma$ ($-z_0$ in Figure 2d]. Instead, we consider an arbitrary phase function of g for the acoustic phase shift by the PA lens (ϕ_{PA}), which is expressed as a function of S/λ:

https://dx.doi.org/10.1021/acsphotonics.0c01313
ACS Photonics XXXX, XXX, XXX−XXX

$$\phi_{PA}(z) = g\left(\frac{S}{\lambda}\right) \quad (5)$$

The separation S in eq 5 takes into account both the axial order change (sign(S)) and the separation (|S|). To verify eq 5, we use a few-cycle pulse modulated by Gaussian envelop for the uniform lateral profile (see the inset of Figure 6). This few-cycle pulse enables us to determine its phase shift of the carrier pulse with respect to the Gaussian envelop. Figure 6 shows the simulated phases (symbols). The fit lines calculated from eq 5 for $\alpha = 0.17$ show a good agreement with the simulated results (COMSOL Multiphysics). By assuming a linear phase function of $g(x) = \alpha x$ with α [rad] being the positive constant, eq 5 is given by $\phi_{PA}(z) = \alpha\frac{S}{\lambda}$.

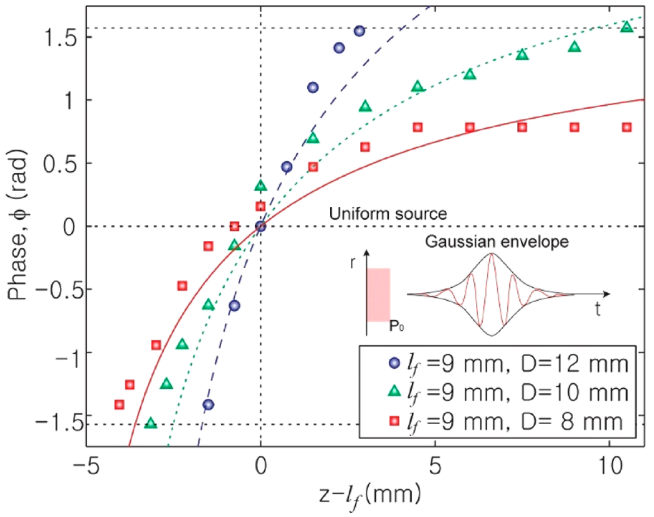

Figure 6. Phase shift (ϕ) as a function of z for a few-cycle pulse modulated by a Gaussian envelop. The uniform later profile is used for the clear separation between z_{EW} and z_{MW}. The symbols indicate the simulation results (COMSOL Multiphysics). The fit lines are obtained from eq 5 for $\alpha = 0.17$ rad.

Phase Shift for Higher Order Beam. Our explanation of the phase anomaly based on the separation and axial order change can be extended to higher-order beams having the phase shifts beyond π.[2,44] As illustrated in Figure 7a, we consider a circularly symmetric, annular photoacoustic beam, $A(r) = \exp\left(\frac{(r-r_p)^2}{r_d^2}\right)$, having the peak intensity at $r = r_p$. According to the Huygens' picture (see Figure 4), the secondary waves originating from the high-intensity sources at $r = r_p$ meet the z axis at $z = z_p$, forming a wavefront at the same location as a result of the interference. The resulting wavefront at $z = z_p$ is located between $z_{MW} = ct$ and z_{EW}. Such spatial separation of z_p from z_{MW} induces an additional phase shift, enabling to exceed a π phase shift. The annular photoacoustic beam is similar to Laguerre−Gaussian (L−G) beams (higher-order Gaussian beam) with the radial mode index $p = 0$, and the azimuthal mode index $l = 1, 2$.[2,45] The resulting phase shift of the L−G beam ($p = 0$) depends on the azimuthal mode index (l), which is given by $(N + 1)\pi = 2\pi, 3\pi$ with $N = l + 2p = 1, 2$.[2] From observation of the higher-order photoacoustic beams, we explain the characteristics of L−G beams: why the phase shifts exceed π and why the phase shift is dependent on the azimuthal mode index.

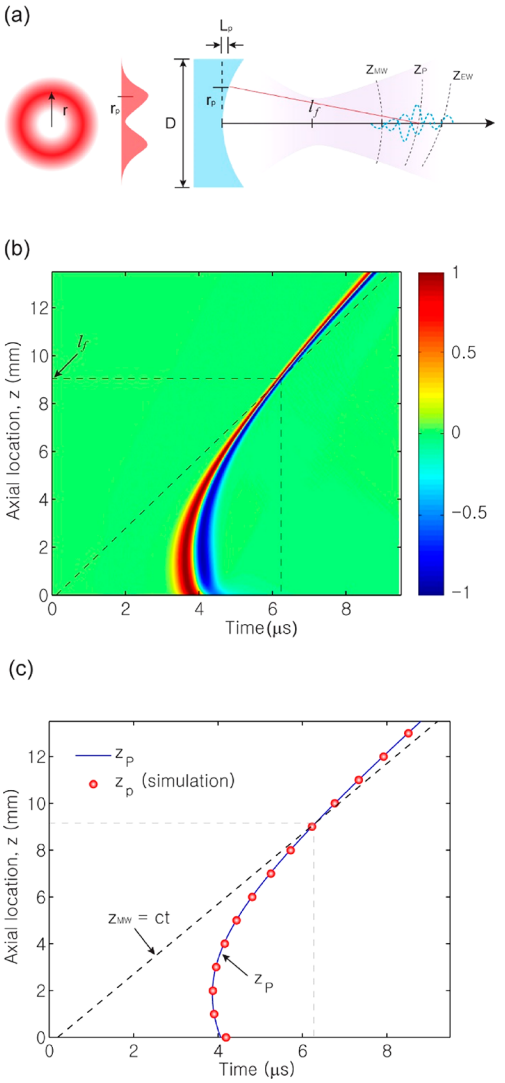

Figure 7. (a) Illustration of the annular (higher-order) photoacoustic beam with a peak intensity at $r = r_p$ and the corresponding reduced depth L_p. Huygens's the secondary waves are exhibited on the z-axis, and the wavefront is formed at $z = z_p$ between $z_{MW} = ct$ and z_{EW}. (b) Axial solutions of the higher-order beam. (c) Locations (z_p) of the wavefront on the z axis. originated from $r = r_p$. The solid line is geometrically calculated by $z_p = L_p + \sqrt{(ct)^2 - (r_p)^2}$, while the symbols are extracted from the axial solutions (b). For comparison, the dashed line represents $z_{MW} = ct$.

Figure 7b shows the simulated axial solution of the higher-order photoacoustic beam of $r_p = 4.5$ mm and $r_d = 1.5$ mm for a PA lens of the same size ($D = 15$ mm and $l_f = 9.2$ mm). We observe that the wave fronts of the annular beam on the z axis (z_p) are deviated from the straight line of $z_{MW} = ct$. Similar to z_{EW}, the wavefront locations z_p are geometrically calculated by $z_p(t) = L_p + \sqrt{(ct)^2 - (r_p)^2}$ with L_p being the reduced depth of the PA lens $L_p = l_f - \sqrt{(l_f)^2 - (r_p)^2} = 1.18$ mm. As seen in Figure 7c, the geometrically calculated $z_p(t)$ (solid line) matches with the simulation results (symbols). We find that the separation (S_{HO}) between z_p and $z_{MW} = ct$ (i.e., $S_{HO} = z_p - z_{MW}$) is related to an additional phase shift, which is given by $\phi_{HO} = 2\pi\frac{S_{HO}}{\lambda}$. For the far field, S_{HO} approaches the reduced

https://dx.doi.org/10.1021/acsphotonics.0c01313
ACS Photonics XXXX, XXX, XXX−XXX

depth L_p, and thus the limit of ϕ_{HO} after the focus is set by the reduced depth L_p, i.e., $\phi_{HO,limit} = 2\pi\frac{L_p}{\lambda}$. For L_p = 1.18 mm and $\lambda = c/f_c$ = 0.3 mm (f_c = 5 MHz), a very large phase shift can be realized, i.e., $\phi_{HO,limit} > 6\pi$. Such a large phase shift well exceeds those of Laguerre−Gaussian beams ($2\pi 3\pi$), because L−G beams have both L_p and r_p comparable to λ,[2] whereas r_p of the PA beams can be arbitrarily chosen. With L_p proportional to r_p, it is understood that a Laguerre−Gaussian beam with a larger azimuthal mode index of l = 2 (thereby larger r_p) has larger phase shift than that with l = 1.

SUMMARY AND DISCUSSION

We have demonstrated the acoustic Gouy phase shift by directly observing the polarity reversal of a focused ultrasound pulse generated by pulsed optical excitation. Unlike the reported works,[26,27] where the acoustic Gouy phase shift of $\pi/2$ was demonstrated, our observation is based on 3D focusing, enabling a π phase shift and polarity reversal. Notably, the polarity reversal by our PA lens features its asymmetric characteristic, because the photoacoustic pulse is emitted from a PA lens (sound baffle). Additionally, our observation is enabled with a relatively low frequency ultrasound (tens of megahertz, $\sim 10^7$ Hz), compared to previously reported observations using a single-cycle picosecond optical pulse (equivalently, terahertz, $\sim 10^{12}$ Hz).

We have explained the physical origin of the Gouy phase shift using Huygens' secondary waves and interference. We find that the polarity of the wave fronts is dictated by the axial sequence change of the secondary waves and the separation relative to the wavelength. For higher order beams, the phase shifts exceeding π can be understood that the axial location of the secondary wave emitted from the peak on a PA lens is deviated from the straight line representing a reference plane wave.

This study not only demonstrates the acoustic polarity reversal, but also provides further understanding of the phase anomaly in optics. Moreover, our observation is based on megahertz ultrasound, also providing a new tool to generate negative monopolar pulses useful for studying interaction of the tensile waves with tissue. The implications of polarity reversal of the megahertz PA pulses can be profound; a full control of the mechanical waves (i.e., pure tensile or compressive pulses) becomes possible, enabling fundamental studies of unit mechanical waves in many areas such as interactions with tissue in ultrasound neuromodulation in the brain,[35,36] mechanotransduction in sensory nerves,[37] and acoustoelectric imaging.[38] Such mechanistic studies based on the unit mechanical waves are considered challenging, because it is extremely difficult to produce a pure tensile wave even with high-performance transducers such as piezoelectric transducers[39] or capacitive micromachined ultrasonic transducers (CMUT) (more than 100% bandwidth).[40]

Experimental Setup. For generation of megahertz photoacoustic pulses, a nanosecond Nd:YAG laser beam (pulse duration 6 ns full-width-half-maximum, Continuum, Surelite I-20) is irradiated on a carbon nanotube (CNT)-polydimethylsiloxane (PDMS) composite coated on the concave side of a optically transparent plano-concave substrate with a 15 mm diameter and a 9.2 mm radius of curvature (a fused silica lens purchased from Optosigma, Inc.). The laser beam was expanded (×5) and collimated before illuminating the CNT-PDMS composite. The CNT-PDMS composite (tens of μm thickness) on the concave surface was prepared by directly growing multiwalled CNTs on the concave surface through a high-temperature chemical vapor deposition process and then coating uncured PDMS solution on the grown CNTs, as the same procedure is found in refs 28, 34. For characterization of photoacoustic pulses, the wave fronts generated in water were visualized by the laser-flash shadowgraph technique.[42] Induced by a local density change due to the compressive/rare-factional waves, contrast images upon back illumination of pulsed dye laser (1 ns) were recorded by a CCD camera (exposure time: ~ms). This imaging technique is a pump−probe method that allows a probe laser pulse (N_2-pumped dye laser, fwhm = 1 ns) to obtain images at a different temporal moment specified by the time delay between the pump (Nd:YAG laser) and the probe pulses through the delay generator (Stanford Research Systems, DG535). In this technique, time-resolved images of the wave propagation can be captured with a time resolution of nanosecond due to the short exposure time of the probe beam (1 ns). A broadband fiber-optic hydrophone (bandwidth up to 75 MHz) was employed to measure the acoustic signals. The hydrophone consists of a single-mode fiber (6 μm core and 125 μm cladding), a continuous diode laser (1310 nm wavelength), and a balanced amplified photodetector (75 MHz bandwidth, Thorlabs). The hydrophone is capable of sensing the acoustic pulses via a change in the light reflection at the fiber/water interface, caused by the pressure-induced refractive index modulation. The modulated signals of the photodetector were monitored by using a digital oscilloscope (WaveSurfer 432, LeCroy, Chestnut Ridge, NY). For bearing high-amplitude pressure pulses near the focus, the tip of the optical fiber is uncoated.

Numerical Simulation. To calculate acoustic propagation, the full wave simulation (axisymmetric) is performed using a finite element method (FEM) solver (COMSOL Multiphysics). The FEM solver solves the time-dependent wave equation, which is given by

$$\frac{1}{\rho c^2}\frac{\partial^2 p}{\partial t^2} + \nabla\cdot\left(-\frac{1}{\rho}\nabla p\right) = 0 \tag{6}$$

where ρ is the density, c is the speed of sound, and ∇ is the vector differential operator (i.e., $\nabla = +\frac{\partial}{\partial x}\mathbf{i} + \frac{\partial}{\partial y}\mathbf{j} + \frac{\partial}{\partial z}\mathbf{k}$ with $\mathbf{i}$, $\mathbf{j}$, and $\mathbf{k}$ being the unit vectors in the x, y, and z coordinates, respectively). The incident pressure field is given by

$$p_0(r, t) = A(r)e^{-t^2/t_d^2} \tag{7}$$

where $A(r)$ is the lateral source pressure profile with r being the distance from the propagation axis, and t_d is the pulse duration ($t_d = 1/2f_c$). The properties of water are used as ρ = 1000 kg/m^3 and c = 1450 m/s. The simulations assume lossless and linear wave propagation.

ASSOCIATED CONTENT

Supporting Information

The Supporting Information is available free of charge at https://pubs.acs.org/doi/10.1021/acsphotonics.0c01313.

The polarity reversal confirmed from the shadowgraph images and the Rayleigh integral, the axial order change of secondary wavelets, correlation of axial spread with phase shift, and calculated phase shifts (PDF)

https://dx.doi.org/10.1021/acsphotonics.0c01313
ACS Photonics XXXX, XXX, XXX−XXX

AUTHOR INFORMATION

Corresponding Author

L. Jay Guo − *Department of Mechanical Engineering and Department of Electrical Engineering and Computer Science, University of Michigan, Ann Arbor, Michigan 48109, United States;* orcid.org/0000-0002-0347-6309; Email: guo@umich.edu

Authors

Taehwa Lee − *Department of Mechanical Engineering, University of Michigan, Ann Arbor, Michigan 48109, United States;* orcid.org/0000-0001-6813-7669

Yeonjoon Cheong − *Department of Mechanical Engineering, University of Michigan, Ann Arbor, Michigan 48109, United States;* orcid.org/0000-0002-8629-8498

Hyoung Won Baac − *Department of Electrical and Computer Engineering, Sungkyunkwan University, Suwon 16419, Republic of Korea;* orcid.org/0000-0001-9295-6162

Complete contact information is available at: https://pubs.acs.org/10.1021/acsphotonics.0c01313

Notes

The authors declare no competing financial interest.

ACKNOWLEDGMENTS

This work is supported by National Science Foundation (CMMI- 1825945). H.W.B. acknowledges the support from the Basic Science Research Program through the National Research Foundation of Korea funded by the Ministry of Education (NRF-2020R1F1A1076828).

REFERENCES

(1) Gouy, L. G. Sur une propriete nouvelle des ondes lumineuses. *C. R. Acad. Sci. Paris* **1890**, *110*, 1251.

(2) Siegman, A. E. *Lasers*; University Science Books, 1986.

(3) Andresen, E. R.; Finot, C.; Oron, D.; Rigneault, H. Spectral analog of the Gouy phase shift. *Phys. Rev. Lett.* **2013**, *110*, 143902.

(4) Boyd, R. W. Intuitive explanation of the phase anomaly of focused light beams. *J. Opt. Soc. Am.* **1980**, *70*, 877.

(5) Feng, S. M.; Winful, H. G. Physical origin of the Gouy phase shift. *Opt. Lett.* **2001**, *26*, 485.

(6) Ruffin, A. B.; Rudd, J. V.; Whitaker, J. F.; Feng, S.; Winful, H. G. Direct Observation of the Gouy Phase Shift with Single-Cycle Terahertz Pulses. *Phys. Rev. Lett.* **1999**, *83*, 3410.

(7) Yang, J.; Winful, H. G. Generalized eikonal treatment of the Gouy phase shift. *Opt. Lett.* **2006**, *31*, 104.

(8) Kuzel, P.; Khazan, M. A.; Kroupa, J. Spatiotemporal transformations of ultrashort terahertz pulses. *J. Opt. Soc. Am. B* **1999**, *16*, 1795.

(9) McGowan, R. W.; Cheville, R. A.; Grischkowsky, D. Direct observation of the Gouy phase shift in THz impulse ranging. *Appl. Phys. Lett.* **2000**, *76*, 670.

(10) Lindner, F.; Paulus, G. G.; Walther, H.; Baltuska, A.; Goulielmakis, E.; Lezius, M.; Krausz, F. Gouy Phase Shift for Few-Cycle Laser Pulses. *Phys. Rev. Lett.* **2004**, *92*, 113001.

(11) Hamazaki, J.; Mineta, Y.; Oka, K.; Morita, R. Direct observation of Gouy phase shift in a propagating optical vortex. *Opt. Express* **2006**, *14*, 8382.

(12) Vaveliuk, P.; Matos, O. M.; Torchia, G. A. Features of the Gouy phase of nondiffracting beams. *Prog. Electromagn. Res.* **2013**, *140*, 599−611.

(13) Martelli, P.; Tacca, M.; Gatto, A.; Moneta, G.; Martinelli, M. Gouy phase shift in nondiffracting Bessel beams. *Opt. Express* **2010**, *18*, 7108−7120.

(14) Pang, X.; Gbur, G.; Visser, T. D. The Gouy phase of Airy beams. *Opt. Lett.* **2011**, *36*, 2492−2494.

(15) Zapata-Rodríguez, C. J.; Pastor, D.; Miret, J. J. Considerations on the electromagnetic flow in Airy beams based on the Gouy phase. *Opt. Express* **2012**, *20*, 23553−23558.

(16) Pang, X.; Visser, T. D. Manifestation of the Gouy phase in strongly focused, radially polarized beams. *Opt. Express* **2013**, *21*, 8331−8341.

(17) Kaltenecker, K. J.; König-Otto, J. C.; Mittendorff, M.; Winnerl, S.; Schneider, H.; Helm, M.; Helm, H.; Walther, M.; Fischer, B. M. Gouy phase shift of a tightly focused, radially polarized beam. *Optica* **2016**, *3*, 35−41.

(18) Baumann, S. M.; Kalb, D. M.; MacMillan, L. H.; Galvez, E. J. Propagation dynamics of optical vortices due to Gouy phase. *Opt. Express* **2009**, *17*, 9818−9827.

(19) Liebmann, M.; Treffer, A.; Bock, M.; Seiler, T.; Jahns, J.; Elsaesser, T.; Grunwald, R. Self-imaging of tailored vortex pulse arrays and spectral Gouy rotation echoes. *Opt. Lett.* **2019**, *44*, 1047−1050.

(20) Erden, M. F.; Ozaktas, H. M. Accumulated Gouy phase shift in Gaussian beam propagation through first-order optical systems. *J. Opt. Soc. Am. A* **1997**, *14*, 2190−2194.

(21) Hariharan, P.; Robinson, P. A. The Gouy phase shift as a geometrical quantum effect. *J. Mod. Opt.* **1996**, *43*, 219.

(22) Yew, E. Y. S.; Sheppard, C. J. R. Fractional Gouy phase. *Opt. Lett.* **2008**, *33*, 1363−1365.

(23) Subbarao, D. Topological phase in Gaussian beam optics. *Opt. Lett.* **1995**, *20*, 2162.

(24) Simon, R.; Mukunda, N. Bargmann invariant and the geometry of the Güoy effect. *Phys. Rev. Lett.* **1993**, *70*, 880.

(25) Zhan, Q. W. Second-order tilted wave interpretation of the Gouy phase shift under high numerical aperture uniform illumination. *Opt. Commun.* **2004**, *242*, 351.

(26) Holme, N. C. R.; Daly, B. C.; Myaing, M. T.; Norris, T. B. Gouy phase shift of single-cycle picosecond acoustic pulses. *Appl. Phys. Lett.* **2003**, *83*, 392.

(27) Kolomenskii, A. A.; Jerebtsov, S. N.; Schuessler, H. A. Focal transformation and the Gouy phase shift of converging one-cycle surface acoustic waves excited by femtosecond laser pulses. *Opt. Lett.* **2005**, *30*, 2019.

(28) Baac, H. W.; Ok, J. G.; Maxwell, A.; Lee, K. T.; Chen, Y. C.; Hart, A. J.; Xu, Z.; Yoon, E.; Guo, L. J. Carbon-nanotube optoacoustic lens for focused ultrasound generation and high-precision targeted therapy. *Sci. Rep.* **2012**, *2*, 989.

(29) Lee, T.; Guo, L. J. Highly Efficient Photoacoustic Conversion by Facilitated Heat Transfer in Ultrathin Metal Film Sandwiched by Polymer Layers. *Adv. Opt. Mater.* **2017**, *5*, 1600421.

(30) Lee, T.; Luo, W.; Li, Q. C.; Demirci, H.; Guo, L. J. Laser-Induced Focused Ultrasound for Cavitation Treatment: Toward High-Precision Invisible Sonic Scalpel. *Small* **2017**, *13*, 1701555.

(31) Lee, T.; Ok, J. G.; Guo, L. J.; Baac, H. W. Low f-number photoacoustic lens for tight ultrasonic focusing and free-field microcavitation in water. *Appl. Phys. Lett.* **2016**, *108*, 104102.

(32) Diebold, G. J.; Sun, T.; Khan, M. I. Photoacoustic monopole radiation in one, two, and three dimensions. *Phys. Rev. Lett.* **1991**, *67*, 3384.

(33) Diebold, G. J.; Khan, M. I.; Park, S. M. Photoacoustic signatures of particulate matter: optical production of acoustic monopole radiation. *Science* **1990**, *250*, 101.

(34) Baac, H. W.; Ok, J. G.; Park, H. J.; Ling, T.; Chen, S. L.; Hart, A. J.; Guo, L. J. Carbon nanotube composite optoacoustic transmitters for strong and high frequency ultrasound generation. *Appl. Phys. Lett.* **2010**, *97*, 234104.

(35) King, R. L.; Brown, J. R.; Pauly, K. B. Localization of ultrasound-induced in vivo neurostimulation in the mouse model. *Ultrasound Med. Biol.* **2014**, *40*, 1512.

(36) Cohen-Inbar, O.; Xu, Z.; Sheehan, J. P. Focused ultrasound-aided immunomodulation in glioblastoma multiforme: a therapeutic concept. *J. Ther. Ultrasound* **2016**, *4*, 17.

https://dx.doi.org/10.1021/acsphotonics.0c01313
ACS Photonics XXXX, XXX, XXX−XXX

(37) Tajik, A.; Zhang, Y.; Wei, F.; Sun, J.; Jia, Q.; Zhou, W.; Singh, R.; Khanna, N.; Belmont, A. S.; Wang, N. Transcription upregulation via force-induced direct stretching of chromatin. *Nat. Mater.* **2016**, *15*, 1287.
(38) Witte, R.; Olafsson, R.; Huang, S. W.; O'Donnell, M. Imaging current flow in lobster nerve cord using the acoustoelectric effect. *Appl. Phys. Lett.* **2007**, *90*, 163902.
(39) Lin, K. W.; Kim, Y.; Maxwell, A. D.; Wang, T. Y.; Hall, T. L.; Xu, Z.; Fowlkes, J. B.; Cain, C. A. Histotripsy beyond the intrinsic cavitation threshold using very short ultrasound pulses: microtripsy. *IEEE Trans. Ultrason. Ferroelectr. Freq. Control* **2014**, *61*, 251.
(40) Xuecheng Jin; Oralkan, O.; Degertekin, F.L.; Khuri-Yakub, B.T. Characterization of one-dimensional capacitive micromachined ultrasonic immersion transducer arrays. *IEEE Trans. Ultrason. Ferroelectr. Freq. Control* **2001**, *48*, 750.
(41) Svelto, O. *Principles of Lasers*; Springer: US, 2010.
(42) Lee, T.; Jang, D.; Ahn, D.; Kim, D. Effect of liquid environment on laser-induced backside wet etching of fused silica. *J. Appl. Phys.* **2010**, *107*, 033112.
(43) Hamilton, M. F. Comparison of three transient solutions for the axial pressure in a focused sound beam. *J. Acoust. Soc. Am.* **1992**, *92*, 527.
(44) Kim, M. S.; Scharf, T.; Assafrao, A. D.; Rockstuhl, C.; Pereira, S. F.; Urbach, H. P.; Herzig, H. P. Phase anomalies in Bessel-Gauss beams. *Opt. Express* **2012**, *20*, 28929.
(45) Allen, L.; Beijersbergen, M. W.; Spreeuw, R. J. C.; Woerdman, J. P. Orbital angular momentum of light and the transformation of Laguerre-Gaussian laser modes. *Phys. Rev. A: At., Mol., Opt. Phys.* **1992**, *45*, 8185.

https://dx.doi.org/10.1021/acsphotonics.0c01313
ACS Photonics XXXX, XXX, XXX−XXX